

Oxygen-vacancy induced structural changes of Co species in CoAl_2O_4 spinels for CO_2 hydrogenation

Yihui Li ^{a,b,1}, Ziang Zhao ^{a,1}, Min Zhao ^c, Hejun Zhu ^{a,*}, Xinzhen Ma ^{a,d}, Zheng Li ^{a,b}, Wei Lu ^a, Xingkun Chen ^d, Linbin Ying ^e, Ronghe Lin ^{d,*}, Yu Meng ^{e,*}, Yuan Lyu ^a, Li Yan ^a, Yunjie Ding ^{a,d,f,**}

^a Dalian National Laboratory for Clean Energy, Dalian Institute of Chemical Physics, Chinese Academy of Sciences, Dalian 116023, China

^b University of Chinese Academy of Sciences, Beijing 100049, China

^c Research Institute of Qilu Petrochemical Company, Sinopec, Zibo 255000, China

^d Hangzhou Institute of Advanced Studies, Zhejiang Normal University, Hangzhou 311231, China

^e Shaanxi Key Laboratory of Low Metamorphic Coal Clean Utilization, School of Chemistry and Chemical Engineering, Yulin University, Yulin 719000, China

^f State Key Laboratory of Catalysis, Dalian Institute of Chemical Physics, Chinese Academy of Sciences, Dalian 116023, China



ARTICLE INFO

Keywords:
 CO_2 hydrogenation
 Selectivity
 CoAl_2O_4
 Oxygen vacancies
 Mechanism

ABSTRACT

Promotional effects of oxygen vacancies of spinel catalysts in CO_2 hydrogenation are reported in early works, but the mechanistic origins remain elusive. Here, CoAl_2O_4 spinels with varying numbers of oxygen vacancies are deliberately designed by a sol-gel method and different post-treatments. By combining catalytic testing, advanced electron microscopic and spectroscopic characterizations, and computational studies, the unusual oxygen vacancy-dependent catalytic behaviors are rationalized. Our work reveals that i) perfect spinel crystals possessing least oxygen vacancies can effectively constrain the Co^{2+} species at working conditions that are less active but selective to CO ; and ii) vacancy-rich spinels promote both H_2 and CO_2 activations and COOH^* formation, explaining the higher hydrogenation activity, but overwhelming vacancies cause Co^{2+} reduction and promote direct CO_2^* dissociation to CO^* and deep hydrogenation to CH_4 . These molecular-level understandings reinforce the idea of proper design of oxygen vacancies to achieve activity-selectivity balance.

1. Introduction

Spinel catalysts of diverse compositions have revealed fascinating prospects among various catalytic reactions [1]. In heterogeneous catalysis, oxygen vacancies play an essential role in determining the catalytic performance. For instance, numerous literatures demonstrate that oxygen vacancies on the surface of spinels are one of the most key defects which can act as the active sites in a range of catalytic reactions, such as CO and CO_2 hydrogenation [2,3], toluene and methane oxidation [4,5], biomass conversion and N_2O decomposition [6,7], etc. Furthermore, the presence of oxygen vacancies on the surface often dramatically changes the adsorption and subsequent reactions of diverse adsorbates considerably, and then affect product selectivity [8–10]. However, full understanding of the crucial functions of oxygen vacancies in the reaction mechanism (e.g., reaction route and

rate-determining step) is severely lacking [11,12]. Deep explorations in this field will shed light on catalytic reaction-promoting effect of oxygen vacancies, which is beneficial to rational catalyst design and implementation for novel catalytic technologies [13,14].

Using CO_2 as a cheap and abundant C_1 raw material to synthesize high-value chemicals could not only alleviate the adverse environmental impacts, but also assist in resolving the energy crisis [15–18]. The syngas ($\text{CO}+\text{H}_2$) obtained by reverse water gas shift (RWGS) reaction is a crucial raw ingredient for chemicals, which could be used to produce an array of liquid fuels and platform chemicals through existing mature processes such as Fischer-Tropsch synthesis and methanol synthesis [19–21]. Usually, the RWGS reaction is accompanied with the formation of C_1 products such as CH_4 and CH_3OH [22,23]. Methanation of CO_2 is a significant catalytic approach to recycling CO_2 emissions into usable fuels with promising commercial applications and environmental

* Corresponding authors.

** Correspondence to: Dalian National Laboratory for Clean Energy, Dalian Institute of Chemical Physics, Chinese Academy of Sciences, Dalian 116023, PR China.

E-mail addresses: zhuhj@dicp.ac.cn (H. Zhu), catalysis.lin@zjnu.edu.cn (R. Lin), mengyu@yulinu.edu.cn (Y. Meng), dyj@dicp.ac.cn (Y. Ding).

¹ These authors contributed equally to this work.

benefits [24–26]. Spinels were widely used as catalyst and support in CO₂ hydrogenation reactions due to the unique properties. For instance, MgAl₂O₄ could serve as a dopant matrix to stabilize small Ni particles, allowing it to exhibit good selectivity in CO₂ methanation reactions [27]. CuAl₂O₄ also exhibits excellent stability in RWGS reaction [28]. ZnAl₂O₄ could be used as a carrier to inhibit sintering of dual-site Cu/ZnAl₂O₄ in CO₂ hydrogenation to methanol [29]. Due to the intricate nature of the CO₂ hydrogenation reaction network, it is critical to understand the mechanistic origins of CO₂ hydrogenation and rationally regulate the catalyst structure in order to generate a single product with high selectivity [30,31].

Oxygen vacancy design of metal oxide catalysts has been emerging as a promising strategy to regulate their catalytic performance in CO₂ hydrogenation. In this aspect, valuable insights have been gathered from the previous studies. The oxygen affinity of oxygen vacancies provides additional adsorption and activation sites for CO₂, which could improve the catalytic activity of CO₂ hydrogenation [13]. The highly inversed spinel catalysts with rich oxygen vacancies were reported to greatly increase the catalytic activity [32]. In addition, oxygen vacancies could also stabilize other active sites for coordinated directional catalysis [33], or promote the generation of stable reaction intermediates such as formates and methoxy species, which were then further hydrogenated to methanol [34] and methane [35], or dissociated to CO [10]. These earlier works mainly focused on improving CO₂ adsorption and activation. Since catalytic reactions often occur around oxygen vacancies with higher CO₂ adsorption capacity, the increased oxygen vacancies may also alter the activation of H₂. A recent study by Fu et al. [36] showed that excessive H₂ activation causes H₂ spillover to non-vacancies and thus affects the catalytic route. Therefore, it is particularly critical to assess the impact of oxygen vacancies on the catalyst structures and the underlying reaction mechanisms.

To tackle the above-mentioned challenge, three representative CoAl₂O₄ spinel catalysts with different numbers of oxygen vacancy structures were prepared through combining a sol-gel method with different post-treatments. The microstructures and in particular the oxygen vacancies of the developed catalysts were deeply analyzed by a spectrum of advanced characterization techniques. The steady-state catalytic CO₂ hydrogenation performances were also fully evaluated and substantiated by in situ spectroscopic and computational studies. Our results showed that the CoAl₂O₄ spinels with perfect crystal facets and least oxygen vacancies could effectively constrain and stabilize the Co²⁺ species in the RWGS reaction, consequently delivering nearly 100% CO selectivity for 100 h even at 500 °C. On the contrary, the analogues with increasing oxygen vacancies facilitated H₂ chemisorption and Co²⁺ reduction, which shifts the hydrogenated product to CH₄. These divergent catalytic behaviors of the spinel catalysts and the underlying hydrogenation mechanisms were discussed and rationalized by joint in situ diffuse reflection infrared Fourier transform spectroscopy (DRIFTS) and density functional theory (DFT) studies.

2. Experimental

2.1. Catalyst preparation

The Co-Al spinels were prepared by a low-temperature sol-gel method (Fig. S1). First, 0.04 mol Al(NO₃)₃·9 H₂O (Aladdin, 99.9%) and 0.02 mol Co(NO₃)₂·6 H₂O (Aladdin, 99.9%) were fully dissolved into 20 mol ethanol (Tianjin Damao Chemical Reagent, 99.7%). The solution was added into 8 mol propylene oxide (Sinopharm Chemical Reagent, 99.0%) at 50 °C with continuous stirring until a Co-Al gel was formed. The gel was then aged for 8 h and dried at 80 °C for 12 h. The dried material was heated at a tube furnace (800 °C, 5 °C/min, 5 h) under either N₂ or air atmospheres, and the derived solids were designated as SPN and SPA, respectively. Additionally, the SPA catalyst was treated by alkali washing to create further oxygen vacancies [32]. The alkaline-treated catalyst was prepared by treating 1.0 g of SPA with 50

mL of a 0.5 M aqueous NaOH solution at 50 °C for 1 h. The resulting suspension was centrifuged, washed thoroughly and then dried at 80 °C for 12 h. The obtained sample was recorded as SPA-NaOH. Lastly, SPN was heated at 600 °C in air (5 °C/min, 5 h) to generate another sample denoted as SPN-A.

2.2. Catalyst characterization

2.2.1. Structural characterization

Thermogravimetric measurements were performed on a STA449F5-Thermostar thermal analyzer in air or N₂ atmospheres with a heating rate of 10 °C/min. Scanning electron microscopic (SEM) images and energy dispersive spectroscopy (EDS) mappings were taken on a JSM-7800 F microscope. High-resolution transmission electron microscopic (HRTEM) images were obtained using a JEOL JEM-2100 electron microscope with 200 kV accelerating voltage. Scanning-transmission electron microscopy (STEM) and the corresponding high-resolution elemental mapping of energy dispersive X-ray (EDX-mapping) images were acquired on a JEM-ARM200F STEM/TEM instrument equipped with Super X EDS, with an instrument resolution of 0.08 nm and an accelerating voltage of 200 kV. The texture of the sample was determined using the Quantachrome Autosorb device and N₂ physisorption. A sample tube containing 50 mg sample was degassed at 200 °C for 6 h before being examined in liquid N₂ at –196 °C. Ex-situ and in-situ X-ray diffraction patterns (XRD) were obtained using a PANalytical X'Pert3 powder diffractometer with Cu K_α radiation at the 30–80° 2θ at a scanning speed of 2°/min. Thermos Scientific Escalab 250Xi device was used to detect the materials' quasi-in-situ and ex-situ X-ray photoelectron spectra (XPS). Raman spectra were collected using a 532 nm excitation wavelength Bruker Optics Senterra Raman confocal microscope spectrometer. The Co-O bond force constant was calculated determined by the Raman shift of the bond according to the Hooke's law ($\omega = \frac{1}{2\pi c} \sqrt{\frac{k}{\mu}}$), where c is light velocity, ω is the Raman shift (cm^{–1}), μ is effective mass, and k is the Co-O force constant [37].

2.2.2. Chemisorption and DRIFTS

CO₂ pulse chemisorption was carried out on an AutoChem 2910 chemical adsorption instrument. Typically, 100 mg catalyst was inserted into a U-shaped sample tube. The sample was initially chilled at 120 °C for 1 h under Ar atmosphere (30 mL/min) and then cooled to 50 °C. Afterwards, a feed of 10% CO₂/Ar was admitted by the pulse gas (loop volume of 526 μL) to saturate the catalyst surface. The physically adsorbed species were removed by purging Ar at the same temperature for 30 min. The desorption was started by ramping the sample temperature to 800 °C at a rate of 10 °C/min, and desorbed products were monitored with a Swiss OminiStar 300 mass spectrometer. H₂ pulse chemisorption was performed on a Zeton Altramira AMI-300 chemical adsorption instrument. 100 mg sample was loaded into a U-shaped tube. The catalyst was first pretreated at 120 °C for 2 h under Ar flow (30 mL/min). After cooling to 50 °C, a 10% H₂/Ar mixture was admitted by pulse injection until adsorption saturation was reached. A thermal conductivity detector was used to detect the desorbed H₂. H₂-D₂ exchange experiments were carried out using an Autochem II 2920 chemisorption fitted with a mass spectrometer. 50 mg catalyst was inserted into U-shaped sample tube, pretreated for 1 h under Ar stream at 120 °C, and then chilled to room temperature. The treatment gas was changed to H₂/D₂ mixture (31 mL/min, D₂/H₂ = 1.07) once the baseline became steady. The temperature was raised to 250 °C with a ramping rate of 5 °C/min. The concentrations of gas-phase components (H₂, D₂, HD) were monitored with a mass spectrometer. In situ diffuse reflection infrared Fourier transform spectroscopy (DRIFTS) experiments were carried out on the VERTEX 80 V FTIR spectrometer. For the in-situ DRIFTS studies of the RWGS reaction, the sample was initially purged with an Ar atmosphere at 120 °C for 30 min before introducing a stream of gas mixture (H₂/CO₂/N₂ = 72/18/10) and ramping the temperature

up to 500 °C at a rate of 5 °C/min.

2.3. Catalytic testing

The reversed water-gas shift reaction was performed in a fixed-bed plug flow reactor equipped with a gas chromatograph. Typically, 0.8 g of catalyst was placed at the center of a quartz tube with an inner diameter of 9 mm. The reaction gases of different H₂:CO₂ ratios were introduced in the absence of pretreatment, with N₂ serving as the internal reference. The performances of various catalysts were evaluated at various reaction temperatures (300–500 °C) under atmospheric pressure. The outlet gas was analyzed online with an Agilent 7890 N GC chromatograph outfitted with a TDX-01 column and a thermal conductivity detector. The CO₂ conversion and product selectivity were estimated by the following equations.

$$\text{CO}_2 \text{ Conversion } (\%) = \frac{n\text{CO}_{2,\text{in}} - n\text{CO}_{2,\text{out}}}{n\text{CO}_{2,\text{in}}} \times 100\%$$

$$\text{CO Selectivity } (\%) = \frac{n\text{CO}_{\text{out}}}{n\text{CO}_{\text{out}} + n\text{CH}_4} \times 100\%$$

$$\text{CH}_4 \text{ Selectivity } (\%) = \frac{n\text{CH}_4_{\text{out}}}{n\text{CO}_{\text{out}} + n\text{CH}_4_{\text{out}}} \times 100\%$$

2.4. Theoretical methods

The theoretical calculation was completed with the Vienna Ab Initio

Simulation Package (VASP) using density functional theory (DFT) method. The key parameters were as follows. The standard pseudopotential of each element in projected augment plane-wave (PAW) method was used. After energy test convergence, the cut-off energy was 450 eV. Because the system contains the magnetic element Co, spin polarization was used in the calculations. For all the structural optimization and property calculations, the convergence thresholds for the energy and force were 10⁻⁵ eV and 0.02 eV/A, respectively. The transition state was found by climbing image nudged elastic band (CI-NEB) method and confirmed by frequency analysis.

3. Results and discussion

3.1. Structural and compositional analyses

CoAl₂O₄ spinels with different numbers of oxygen vacancies were prepared by the sol-gel method using corresponding metal nitrates as the precursors in the presence of propylene oxide (procedures illustrated in Fig. S1). To create more oxygen vacancies, the dried solids from the resulted gels were treated by different methods. Direct heating of the solids in flowing air or N₂ at 800 °C yielded the reference CoAl₂O₄ spinels that were denoted as SPA and SPN, respectively. Additional two samples were derived by different treatments of these two compounds. SPN was further oxidized in air at 600 °C to yield a sample coded as SPN-A. Meanwhile, SPA was subject to NaOH etching at a mild temperature of 50 °C to create a new sample denoted as SPA-NaOH. Thermogravimetry (TG) was performed on the precursor Co-Al gel and the

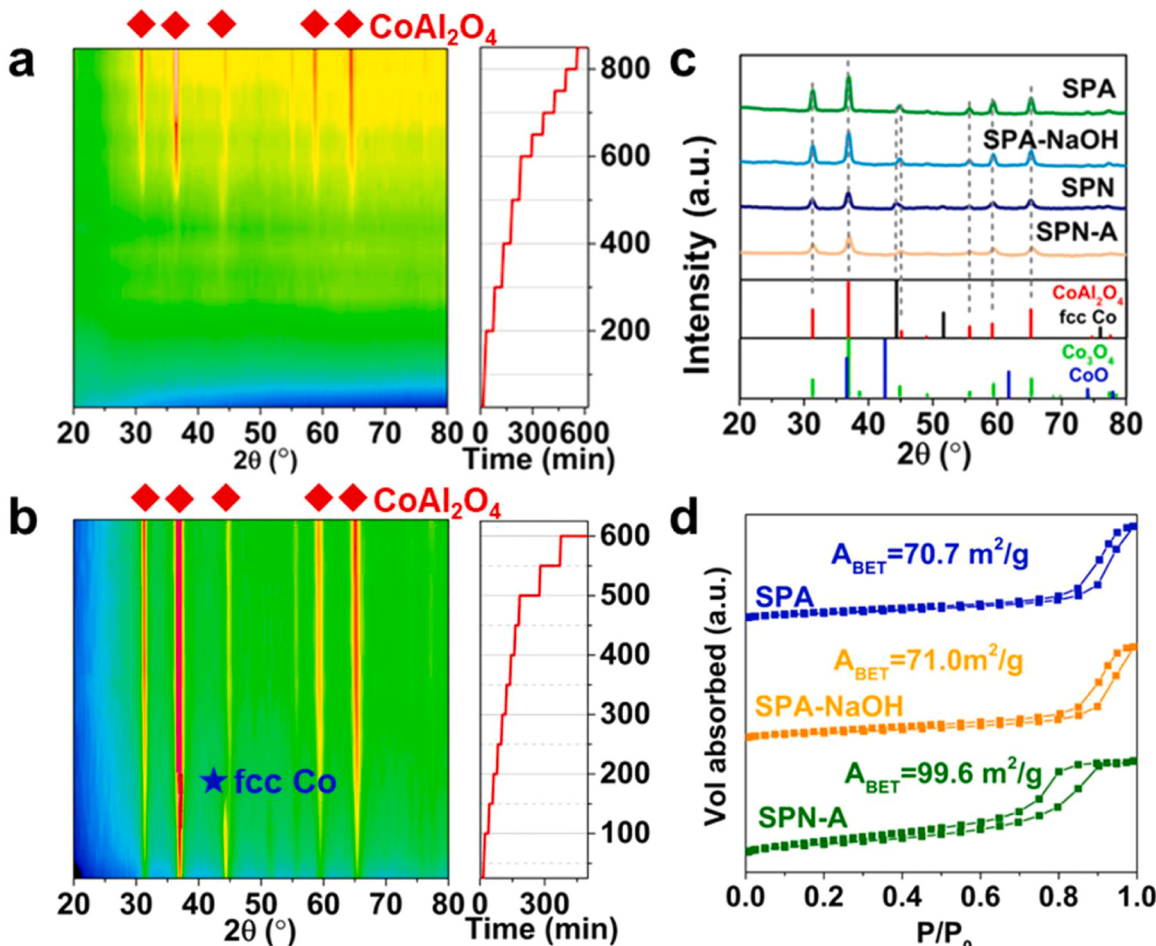


Fig. 1. In situ XRD patterns of (a) Co-Al precursor in Air and (b) SPN in Air. (c) The XRD patterns of the SPA, SPA-NaOH, SPN and SPN-A catalysts, and the standard references of CoAl_2O_4 , Co_3O_4 , CoO and fcc Co (vertical lines). (d) N_2 sorption isotherms of the different CoAl_2O_4 spinel catalysts.

exhaust gas was detected by mass spectrometry to explore the chemical changes of the Co-Al precursor during the heat treatment process in Fig. S2. It was found that the H_2 peak was found at a higher temperature during the programmed temperature rise under N_2 , which may be due to the hydrogen element in the precursor being generated under oxygen-poor conditions, thus promoting the generation of Co^0 . Under Air atmosphere, no H_2 peak was found due to oxygen enrichment. The phase evolution of the solid gels during oxidation in air ambience was studied by *in situ* XRD with temperature-programmed heating mode (Fig. 1a). The characteristic diffraction patterns of $CoAl_2O_4$ appeared at 400 °C after air oxidation, and these characteristics became more intense at the increasing temperatures up to 800 °C. In addition, the temperature-programmed phase evolution of SPN in air was also explored through *in situ* XRD (Fig. 1b). Differing from the diffraction patterns of SPA that showed the exclusively phase of $CoAl_2O_4$, metallic Co with fcc packing was evidenced for SPN, hinting the prominent impact of heating atmospheres on the phase transformation. The diffraction lines of the fcc Co gradually vanished and completely disappeared at 250 °C, accompanied with the formation of $CoAl_2O_4$ spinels. Clearer single spectra before and after key changes in the *in situ* XRD spectrum are also provided in Fig. S3. To have a better comparison on the structures of the derived catalysts, their respective XRD patterns are presented in Fig. 1c. Although the XRD patterns for the catalysts clearly indicated the presence of only $CoAl_2O_4$ crystallites (JCPDS card: 01-082-2248), still, noticeable differences were observable among these catalysts. While SPA-NaOH remained essentially unaltered in crystallinity as compared with SPA, SPN-A clearly displayed much lower diffraction intensities. The relative crystallinity of the different catalysts estimated by XRD patterns was in the order of SPA (100) > SPA-NaOH (97.1) > SPN-A (74.3). Next, the porosities of the above derived samples were analyzed

by N_2 sorption (Fig. 1d and Table S1). While both SPA and SPA-NaOH possessed similar specific surface areas (S_{BET}) of ca. 71 m^2/g , SPN-A showed a higher value of 99.6 m^2/g , implying that the post-oxidation maybe beneficial to generate more defective structures.

3.2. Electron microscopic studies

Having confirmed the compositions of the developed catalysts, combined electron microscopic investigations were performed to visualize the morphologies and particle sizes of the key samples (Fig. 2). The low-resolution TEM images showed more crystallized particles for both SPA and SPA-NaOH than SPN-A that displaying obvious amorphization (Fig. 2a-c). Statistic counting of the particles showed that the average sizes of $CoAl_2O_4$ were 16.0, 15.6 and 8.5 nm, respectively, for SPA, SPA-NaOH, and SPN-A, thus corroborating well with the crystallite sizes estimated by Scherrer equation (Table S1). The size of the $CoAl_2O_4$ catalyst often affects the catalytic performance including catalyst reduction and catalytic activity [38]. HRTEM images of the catalysts illustrate the distinctive lattice distances of 0.468, 0.286, and 0.244 nm (Fig. 2d-f), corresponding to the respective (111), (220) and (311) planes of $CoAl_2O_4$ with SPA, SPA-NaOH and SPN-A catalysts. The characteristic lattice fringes of fcc Co (111) with $d = 2.05$ nm were also observed in the SPN catalyst in Fig. S4, which is consistent with the *in-situ* XRD, indicating that the original reduction was achieved under N_2 calcination. Furthermore, the two-dimensional projections of SPA generally present hexagonal grains with clear boundaries and complete lattice stripe orientation, implying that the SPA grains are similar to single crystals in the cubic system with perfect crystal facet. In contrast, for SPA-NaOH, due to the destruction of the crystalline integrity by alkaline etching, more defects appeared at the corners and edges of the

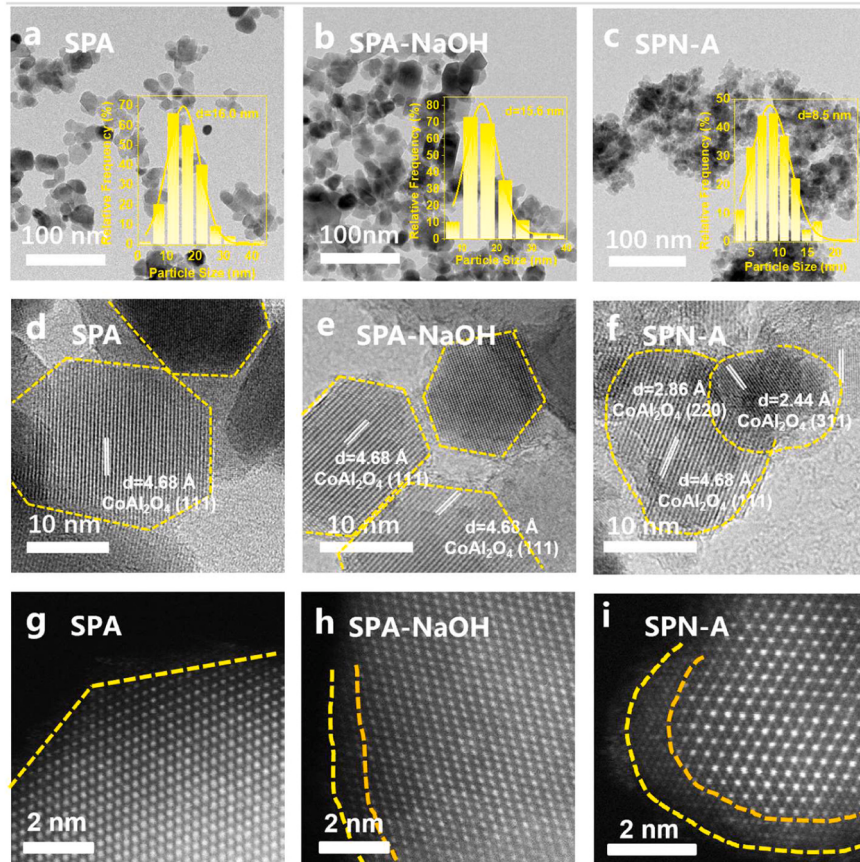


Fig. 2. Electron microscopic characterizations of the three $CoAl_2O_4$ catalysts. (a-c) TEM images and the particle size distributions (insets) (d-f) HRTEM images, showing the representative lattice fringes of different Co species. (g-i) HAADF-STEM images, revealing the differences of defective sites on the particle edges.

hexagonal grains, and the boundaries became blurred albeit the lattice fringes in the grains remained intact (Fig. 2e). These observations confirmed that SPA-NaOH was mainly composed of single crystal grains, but many defects were formed on the grain surface or edge. For SPN-A, the grain boundaries became well-rounded and thus more disordered (Fig. 2f). High-index facets such as (220) and (311) coexisted with the typical (111) facets, forming nanoscale crystal defects such as steps, corners, and depressions, and thus confirming polycrystalline characteristics of the grains [39,40]. HAADF-STEM was further applied to visualize the detailed defective structures (Fig. 2g-i). The grain boundaries of SPA-NaOH and SPN-A were incomplete and disordered layers with a thickness of 1–2 nm were observed, which can be attributed to the exfoliation of surface lattice oxygen during the base or oxidation processing [41]. In addition, SEM images and EDS mapping of different catalysts revealed that all the catalysts were evenly distributed (Figs. S5–S6).

3.3. Oxygen vacancies

Since the catalytic reaction occurs on the surface, the surface properties of the catalysts were studied by XPS (Fig. 3a). The Co 2p XPS spectra of the three pre-reaction catalysts are shown in Fig. S7. Only the characteristic binding energy peak of Co^{2+} was found. Comparison on the O 1s XPS spectra of the three catalysts revealed that the peak of SPN-A noticeably shifted towards higher binding energy as compared with the other two catalysts. Following the previous literature [32], the O 1s envelopes were deconvoluted into two peaks: lattice oxygen (O_L) on the surface and adsorbed oxygen on the surface (O_A), and the formation of oxygen vacancies due to O_2 adsorption. The fitting results of the three samples revealed that the $\text{O}_\text{A}/(\text{O}_\text{A}+\text{O}_\text{L})$ ratios follow the order of SPN-A > SPA-NaOH > SPA. Therefore, the formation of more oxygen vacancies in SPN-A with a more disordered spinel structure corresponds to the irregular surface defects of the catalyst. To further study the crystal structure of CoAl_2O_4 catalysts, Raman spectroscopy was performed (Fig. 3b). CoAl_2O_4 typically presents five active Raman models: F_{2g} (201, 516, 615 cm^{-1}), E_g (406 cm^{-1}) and A_{1g} (705 cm^{-1}) [39,42]. Among them, the F_{2g} (1) mode belongs to Co/Al-O₄ tetrahedral translation. The E_g mode corresponds to the symmetric bending motion of the oxygen atom in the tetrahedron, and its position has a decent association with the cation radius of the 8a site. [43]. The Co/Al-O asymmetric stretching vibrations in the tetrahedral sites are responsible for the F_{2g} (2) mode. The F_{2g} (3) mode is the antisymmetric stretching mode of the tetrahedral unit and the asymmetric bending motion of the oxygen bonded to the tetrahedral cation. The Co/Al-O stretching vibration in the octahedron is related to the A_{1g} mode. F_{2g} (2) can be viewed as the evidence for judging the existence of metal-O bonds in spinels [43]. It was found that the F_{2g} (2) peaks of SPA, SPA-NaOH and SPN-A catalysts located at 522.8, 520.9 and 517.4 cm^{-1} respectively, indicating red-shifting with the increasing oxygen vacancies. According to the Raman shift of the Co-O bond, the

bond force constant (K) of Co-O bond was calculated, following the order of SPN-A < SPA-NaOH < SPA (Fig. 3b). An interesting quasi-linear relationship was established between the relative O_A content and the bond force constant (Fig. S8), illustrating that the increasing O_A concentration leads to the weakening of the Co-O bond of the spinel catalyst [37].

3.4. CO_2 hydrogenation

The CoAl_2O_4 spinels with different structures were evaluated for CO_2 hydrogenation reaction in a fixed bed reactor at 300–500 °C (Fig. 4a). SPA displayed a moderate CO_2 conversion with almost full CO selectivity at 400 °C. Both the conversion and CH_4 selectivity increased slightly on SPA-NaOH. In contrast, the CO_2 conversion significantly improved over SPN-A and CH_4 became the predominate product with a higher selectivity of 90%. The impacts of temperature and H_2/CO_2 ratio on the product selectivity and CO_2 conversion were further evaluated. The CO selectivity of SPA catalyst kept at ~100% in the full temperature range of 300–500 °C (Fig. 4g) and remained stable in the 100 h time-on-stream (Fig. 4b). The stability test of SPN-A reveals that the CH_4 selectivity increased and became stable after 15 h (Fig. 4b). The CO selectivity of SPN-A catalyst increased slightly as the temperature increased from 400 to 500 °C, but CH_4 was still the major product (Fig. 4g). The effect of H_2/CO_2 ratio on the catalytic performance was presented in Fig. 4h. As expected, a higher H_2/CO_2 ratio promoted CO_2 conversion, but the impact on product distribution varied. The CO selectivity remained ~100% on SPA at $\text{H}_2/\text{CO}_2 = 4$, whereas CH_4 formation was enhanced over SPA-NaOH and SPN-A with the increasing H_2/CO_2 ratio. Subsequently, the electronic states of the Co species in different catalysts after the reaction were detected. The XRD patterns of the spent catalysts show that the CoAl_2O_4 spinel was stable on SPA after the reaction (Fig. 4c). In contrast, the spent SPN-A showed the characteristic peak of fcc Co in addition to CoAl_2O_4 , indicating that the active centers of the catalyst might comprise both nanoparticle of Co^0 and CoAl_2O_4 during the reaction. Quasi in situ XPS investigation of two spent catalysts further revealed that SPN-A was partially reduced to metallic Co nanoparticle, whereas the Co^{2+} species on SPA remained stable in the H_2/CO_2 reaction atmosphere (Fig. 4d) and it was found that the spent catalyst has more oxygen vacancies (Fig. S9). These results were further corroborated by HRTEM analyses (Fig. 4e-f), confirming the exclusive presence of CoAl_2O_4 on SPA, but small metallic Co nanoparticles coexisting with CoAl_2O_4 on SPN-A. The SPN-A catalyst was tested after H_2 reduction to demonstrate the active center which produced CH_4 (Fig. S10). It was discovered that the CH_4 selectivity could be raised to 98%, thus confirming that active center was Co^0 species obtained by CoAl_2O_4 reduction. The reaction-induced partial phase transition from CoAl_2O_4 to Co^0 in SPN-A can well explain the induction phenomenon during the stability test (Fig. 4b).

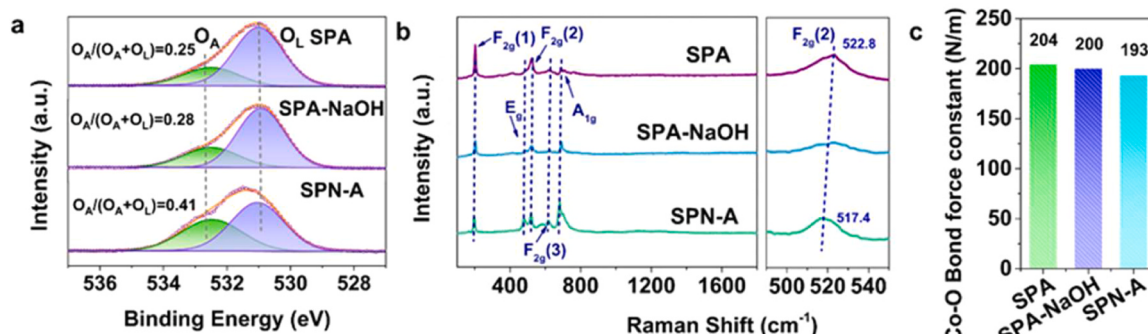


Fig. 3. (a) The O 1s XPS spectra, and (b) Raman spectra of the different CoAl_2O_4 spinel catalysts. (c) The calculated Co-O bond force constants based on the Hooke's law.

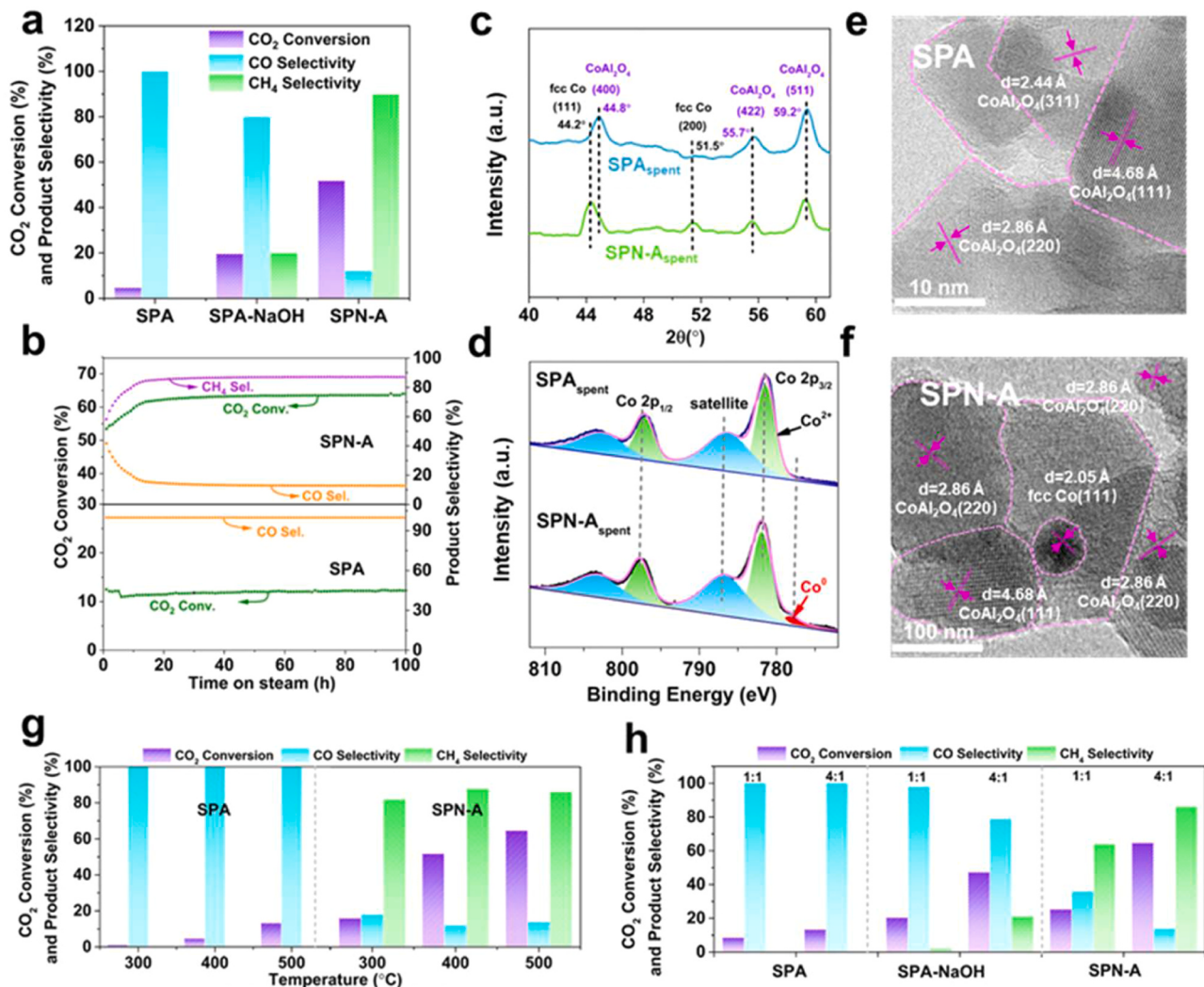


Fig. 4. (a) Catalytic performance of CoAl_2O_4 catalysts in CO_2 hydrogenation. (Reaction conditions: $400\text{ }^\circ\text{C}$, 0.1 MPa , $5000\text{ mL}\cdot\text{g}^{-1}\cdot\text{h}^{-1}$, $\text{H}_2/\text{CO}_2/\text{N}_2 = 72/18/10$). (b) 100 h time-on-stream of the SPA catalyst (Reaction condition: $500\text{ }^\circ\text{C}$, 0.1 MPa , $5000\text{ mL}\cdot\text{g}^{-1}\cdot\text{h}^{-1}$, $\text{H}_2/\text{CO}_2/\text{N}_2 = 72/18/10$). (c) XRD patterns of the different spent catalysts. (d) Co 2p XPS spectra of the spent catalysts. TEM images of the spent (e) SPA and (f) SPN-A catalysts. CO_2 conversion and product selectivity at different (g) temperatures (0.1 MPa , $5000\text{ mL}\cdot\text{g}^{-1}\cdot\text{h}^{-1}$, $\text{H}_2/\text{CO}_2/\text{N}_2 = 72/18/10$) and (h) H_2/CO ratios ($500\text{ }^\circ\text{C}$, 0.1 MPa , $5000\text{ mL}\cdot\text{g}^{-1}\cdot\text{h}^{-1}$).

3.5. Reduction and chemisorption properties

$\text{H}_2\text{-TPR}$ profiles of the different CoAl_2O_4 catalysts were recorded and represented in Fig. 5a. No reduction peak was observed on SPA up to $700\text{ }^\circ\text{C}$, while two high-temperature reduction peaks were found on SPN-A and SPA-NaOH, which can be attributed to the reduction of surface and bulk Co species, respectively [44,45]. The reduction temperatures for SPN-A catalyst were 411 and $520\text{ }^\circ\text{C}$, respectively. These peaks shifted to 520 and $780\text{ }^\circ\text{C}$ for SPA-NaOH. According to the previous literature [46], the shifting toward higher reduction temperature could be ascribed to the presence of stable oxide species that are hard to reduce. The higher portion of the low-temperature reduction peak in SPN-A thus corroborates with the most abundant oxygen vacancies as revealed by our combined characterizations. In addition, H/D exchange experiments showed that the light-off curves of HD formation shifted to the lower temperatures in the order of SPA > SPA-NaOH > SPN-A (Fig. 5b). The results show that the increase in oxygen vacancies enhances the ability to activate H_2 , which promotes catalyst reduction, and the catalytic products are more inclined to further hydrogenation. To this end, H_2 pulse adsorption experiments were conducted to evaluate the H_2 adsorption/activation ability of the different catalysts [47,48]. The H_2 pulse adsorption experiments of the catalysts show that the

increase in oxygen vacancies promotes the adsorption of H_2 (Fig. 5c). For instance, the H_2 adsorption capacity of SPA was $10\text{ }\mu\text{mol/g}$ and that of SPN-A increased to $30\text{ }\mu\text{mol/g}$. Similar results were acquired for the CO_2 adsorption experiments. The CO_2 adsorption quantities were determined to be 4.6 , 19.2 and $33.9\text{ }\mu\text{mol/g}$, respectively, for SPA, SPA-NaOH and SPN-A (Fig. 5d). Note that the different CO_2 adsorption intensities between these catalysts can affect the activation of hydrogen, thus further influencing the adsorption/desorption of active intermediates and product selectivity [34,49].

3.6. In situ DRIFT study

In situ DRIFTS was performed under RWGS reaction conditions to explore the kinetic fingerprints (Fig. 6 and S11), and the corresponding band assignments were listed in Table S2. In a mixed atmosphere ($\text{H}_2/\text{CO}_2/\text{N}_2 = 72/18/10$) the sample temperature was elevated over SPA (Fig. 6a), SPA-NaOH (Fig. 6b) and SPN-A (Fig. 6c), respectively. On SPA and SPA-NaOH, the formations of COOH^* (carboxylates) and CO_3^* intermediates were first observed at 1657 and 1434 cm^{-1} , indicating that the catalysts first underwent CO_2 adsorption to generate CO_3^* and COOH^* intermediates. The peak intensities of two intermediates decreased significantly with the increasing temperatures, accompanied

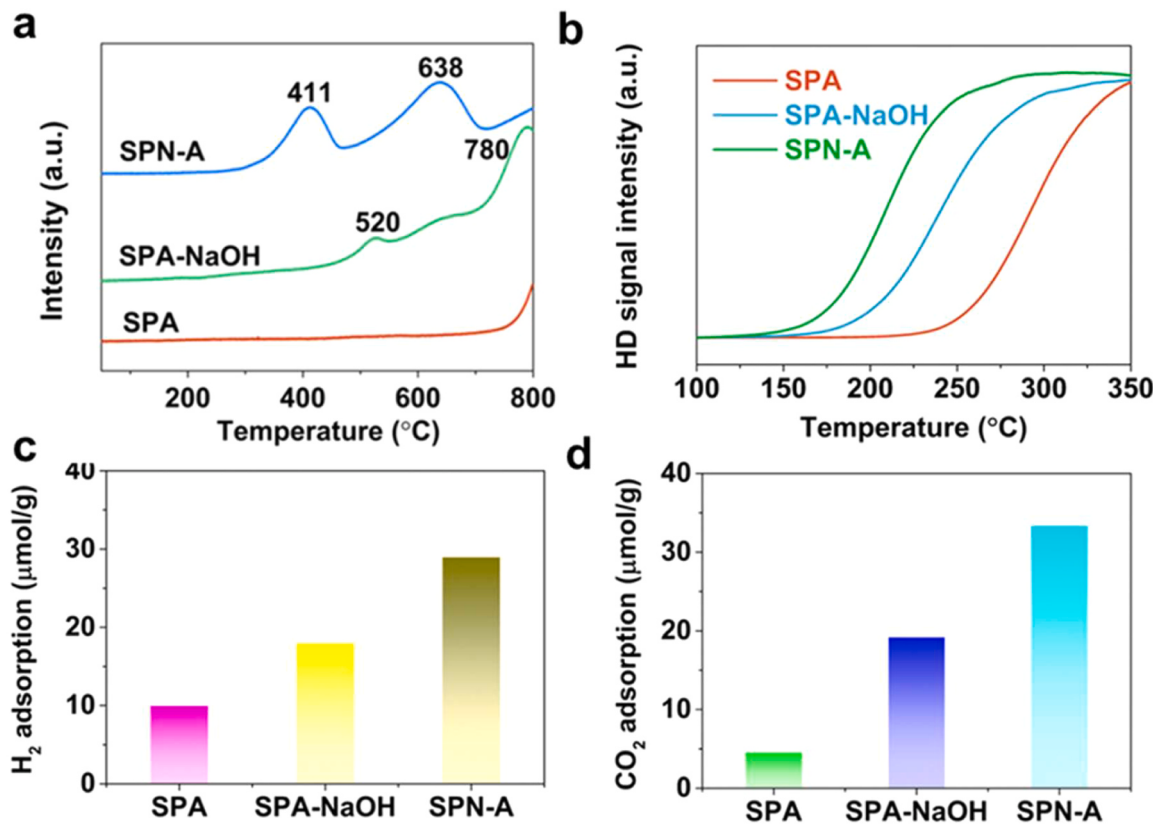


Fig. 5. (a) H₂-TPR, (b) H₂-D₂ exchange, (c) H₂ adsorption and (d) CO₂ adsorption on the three CoAl₂O₄ catalysts.

by the gradual formation of CO, which indicated that the intermediates COOH* and CO₃* were gradually consumed at higher temperatures to generate gas-phase CO [50]. A comparison on the temperatures corresponding to the release of gas-phase CO between SPA and SPA-NaOH (approximately 420 and 350 °C, respectively) reveals a lower temperature for SPA-NaOH, agreeing well with the higher hydrogenation activity as described previously. In addition, with the further increasing of temperatures, the C-H stretching vibration bands of HCOO* (formates) intermediates at 2762, 2903 and 2997 cm⁻¹ and the C-O stretching vibrations at 1593 and 1303 cm⁻¹ were also observed, indicating that the HCOO* intermediates were more difficult to generate and desorb than the COOH* intermediates and in good agreement with the earlier studies [27,51]. In the Ar purge experiments, it was found that the HCOO* intermediate was more difficult to desorb on SPN-A and SPA-NaOH, and the characteristic peak of HCOO* was still observable after 30 min purging, indicating that the generated HCOO*-intermediate was difficult to undergo further reactions (Fig. S12). On SPN-A, the generation and consumption of COOH* with increasing temperatures were also evidenced, accompanied with the release of CO. Nonetheless, in addition to the gas-phase CO, the surface-bound CO* intermediate species appeared at 2006 cm⁻¹ at a low temperature of 150 °C. This CO* intermediate red-shifted to 1952 cm⁻¹ when the temperature increased. In addition, the characteristic bands of the HCOO* intermediates appeared at 200 °C, but the intensities decreased with the increasing temperatures, accompanied with the formation of meteorological CH₄ (3014, 1226 cm⁻¹). Therefore, the formation of CH₄ may be from CO* and HCOO*. Ar purge experiments further showed that the CO* was easier to desorb than HCOO*, hinting that CH₄ was more likely originated from the hydrogenation of the CO* intermediates.

3.7. Mechanistic insights

To clarify the relationships between different oxygen vacancies of CoAl₂O₄ and the selectivity to CO and CH₄ during CO₂ hydrogenation, DFT calculations were performed, with the focus placed on the adsorption of key intermediate species generated in CO₂ hydrogenation and the reaction mechanism. Based on our thorough characterizations, three different Co catalyst models were constructed for SPA, SPA-NaOH and SPN-A, considering the different cobalt compositions (nano-particle metallic Co and CoAl₂O₄) and CoAl₂O₄ with or without oxygen vacancies (Figs. S13-S14). For the rational selection of oxygen vacancy-bearing spinels, the formation energies were first computed for the different faceted CoAl₂O₄ with oxygen defects (Fig. S13) and Table S3). The (100) facet with the lowest energies of 2.5 eV was thermodynamically more favorable than the (111) and (110) facets (4.26 and 3.76 eV, respectively), and thus was chosen for further consideration. The full reaction coordinates of the simulated elemental steps of CO₂ hydrogenation over CoAl₂O₄(100), CoAl₂O₄-O_v(100) and Co(111) were presented in Fig. 7. The CO₂ adsorption at both CoAl₂O₄(100) and CoAl₂O₄-O_v(100) was exothermic and more favorable for the latter, agreeing well with the CO₂ chemisorption analysis. Afterwards, the activation of CO₂* underwent an upwards slope with the energy barriers of 1.18 and 1.09 eV, respectively. The subsequent hydrogenation of the adsorbed CO₂* and H-assisted dissociation can generate either HCOO* or COOH* intermediates. Although both routes are energy-demanding irrespective of the oxygen vacancies, the COOH* route is kinetically more favorable with much lower barriers, particularly for CoAl₂O₄-O_v(100) with the lowest barrier of only 0.34 eV. After passing another transient state (TS), these adsorbed COOH* intermediates further dissociate into CO* with only 0.16–0.35 eV. Due to the relatively weak adsorption of CO*, it will directly desorb into gas-phase CO instead of going further hydrogenation that requires higher energy input. For Co(111), the energy barrier for the direct dissociation of CO₂ to form CO* is

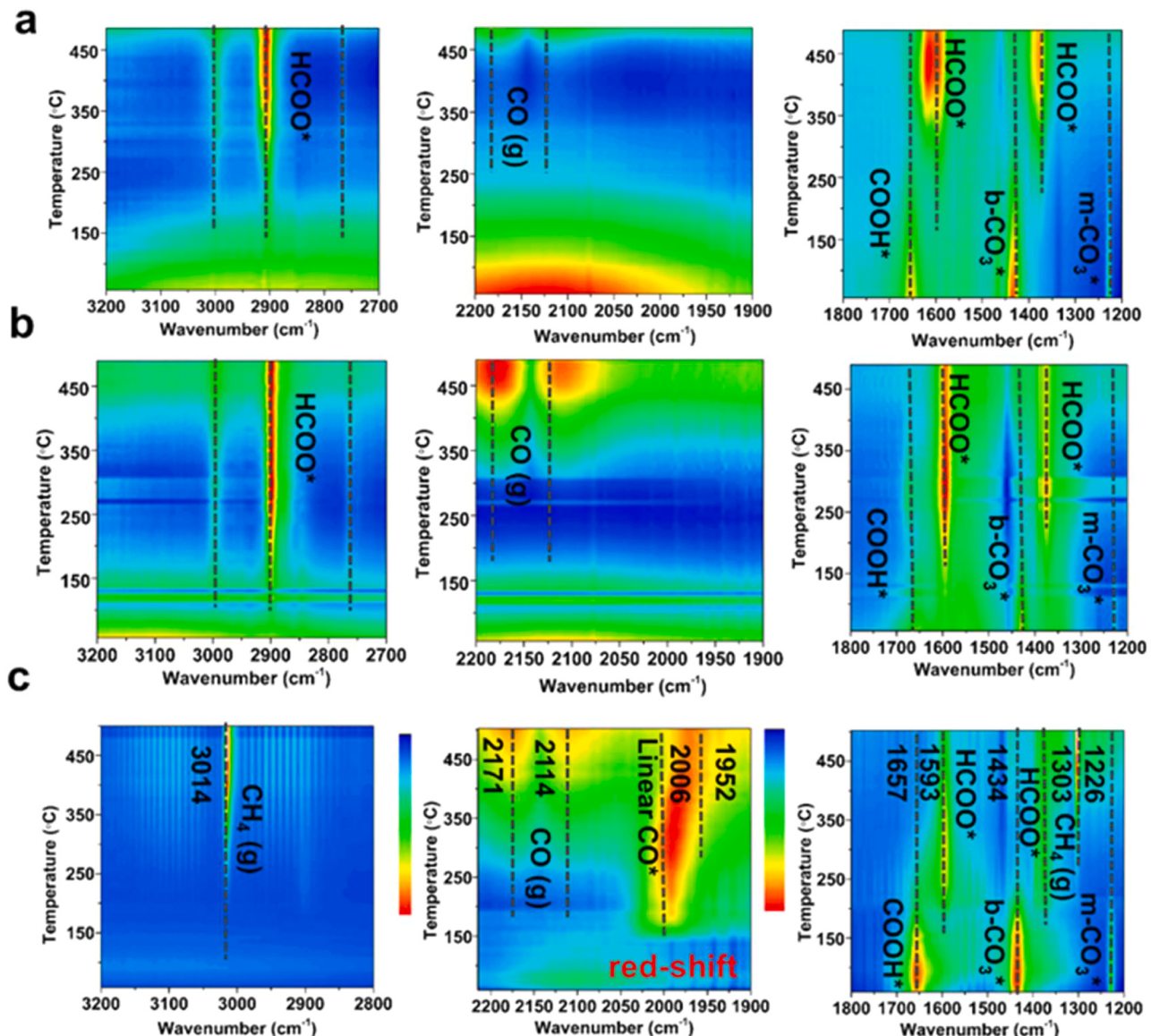


Fig. 6. In situ DRIFTS spectra of (a) SPA, (b) SPA-NaOH and (c) SPN-A catalysts after exposure to the gas mixture ($H_2/CO_2/N_2 = 72/18/10$) at different temperatures during CO_2 hydrogenation.

lower as compared with COOH^* and HCOO^* , and the energy barrier for further hydrogenation of CO^* is lower than the desorption energy barrier, so it is easier for further hydrogenation to CH_4 (Fig. 7c). The full adsorption configurations on the three model catalysts are shown in Figs. S15-S17 for reference. In general, the DFT calculations are in good agreement with the activity and product selectivity of the different Co species in the CO_2 hydrogenation experiment.

3.8. Roles of oxygen vacancies

The multifaceted roles of oxygen vacancies in CO₂ hydrogenation have been reported by different research groups [10,13,17]. Even so, the mechanistic origins behind these observed phenomena are mainly speculated. By constructing three CoAl₂O₄ spinels with varying numbers of oxygen vacancies, their critical roles in hydrogenation performance were systematically assessed in this study as summarized in Fig. 8. In the earlier literatures, the oxophilic nature of oxygen vacancies were reported to enhance the adsorption of CO₂, and subsequently the hydrogenation was facilitated at the adjacent metal atoms [32]. These conclusions were fully supported by our CO₂-TPD and catalytic

evaluations. Nonetheless, the enhanced CO_2 adsorption might not be the only reason accounting for the improved activity. In fact, our DFT calculations revealed only slight differences in the CO_2 activation between $\text{CoAl}_2\text{O}_4(100)$ with or without oxygen vacancies (barriers of 1.09 and 1.18 eV, respectively). In stark contrast, the H-assisted activation of CO_2^* to COOH^* , which is the rate-limiting step on $\text{CoAl}_2\text{O}_4(100)$ with a high barrier of 1.37 eV, is significantly favored on $\text{CoAl}_2\text{O}_4(100)\text{-O}_v$ with a mild barrier of only 0.34 eV. This suggested that the splitting of molecular H_2 is also crucial to the above elemental step. This speculation was indeed supported by our H_2 -TPD and H/D exchange experiments, i. e., the H_2 adsorption and activation propensities scale with the increasing numbers of oxygen vacancies. In addition, the increasing oxygen vacancies were found to impact the reducibility of the Co^{2+} species that has scarcely been addressed in early works. Albeit CO_2 hydrogenation activity can be promoted on oxygen vacancy-rich CoAl_2O_4 spinels, while product selectivity from CO to CH_4 was evidenced on SPN-A with the most abundant oxygen vacancies. This was clearly ascribed to the reduction of CoAl_2O_4 spinels to metallic Co species in the hydrogenation atmosphere, which has been confirmed by the characterization of the post-reaction catalyst. Supported by both *in situ*

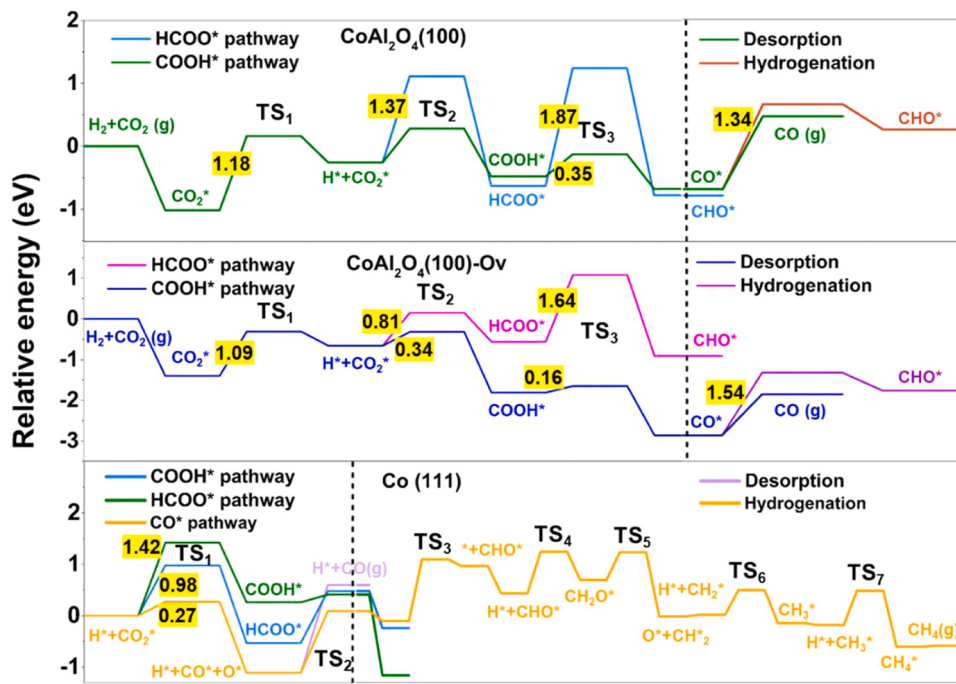


Fig. 7. The full reaction coordinates of CO_2 hydrogenation on the different Co-based model catalysts: (a) $\text{CoAl}_2\text{O}_4(100)$, (b) $\text{CoAl}_2\text{O}_4(100)\text{-Ov}$, and (c) $\text{Co}(111)$.

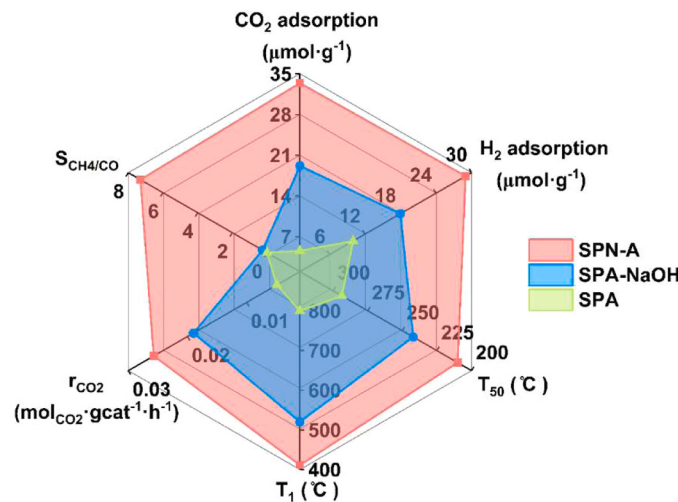


Fig. 8. Performance descriptors in CO_2 hydrogenation on different Co-based catalysts: SPA, SPA-NaOH and SPN-A. The pink, blue and green shaded areas represent the descriptors for SPN-A, SPA-NaOH and SPA, respectively. T_{50} : the temperature corresponding to 50% HD exchange activity; T_1 : the temperature of the first reduction peak in $\text{H}_2\text{-TPR}$, where 800 °C for SPA represents greater than 800 °C; r_{CO_2} : hydrogenation rate; $S_{\text{CH}_4/\text{CO}}$: the ratio of CH_4 selectivity to CO selectivity.

DRIFT and DFT calculations, these in situ generated Co^0 species was proved to facilitate the direct hydrogenation of the CO_2^* to CO^* instead of the COOH^* on CoAl_2O_4 irrespective of the oxygen vacancies, thus providing the mechanistic basis for the underlying reaction mechanisms. On the other hand, the strongly promoted reduction behaviors of CoAl_2O_4 spinels by the creation of oxygen vacancies might be associated with the greatly enhanced H_2 adsorption and activation. The recent report by Bao et al. [36] suggested the remote H-spillover from ZnO to Co_3O_4 which promoted the reduction of the latter. However, such phenomenon was not detected when small Co_3O_4 particles were constrained by the $\text{ZnO}\text{-Co}_3\text{O}_4$ interface. We speculate that the less constrained Co^{2+}

species due to the creation of oxygen defects led to easier reduction of CoAl_2O_4 spinels.

4. Conclusions

In this study, we have developed three Co-Al spinel catalysts containing varying numbers of oxygen vacancies by a sol-gel method and different post-treatments. The detailed structural and compositional information as well as the differences in oxygen vacancies were fully characterized by combined microscopic and spectroscopic techniques. The impacts of the oxygen vacancies on their CO_2 hydrogenation performances were systematically evaluated. These experiments enabled to acquire new fundamental insights into the unveiled mechanistic of the oxygen vacancy-dependent catalytic responses, i.e., exclusive CO formation with lower activity on perfect spinel crystals possessing least oxygen vacancies, and highly active but CH_4 -selective spinels with overwhelmingly rich oxygen vacancies. This unusual phenomenon can be associated with the different stabilities of the Co^{2+} species that were more susceptible to reduction during working conditions wherein the O defective sites enriched the adsorption and activation of H_2 . Therefore, there is a complex interplay between the oxygen vacancies of the spinels, the catalyst stability (under reductive atmospheres), and the hydrogenation performance, which ultimately calls for more careful catalyst design.

CRediT authorship contribution statement

Yihui Li: Investigation, Data curation, Conceptualization, Formal analysis, Methodology, Visualization, Writing - original draft. **Ziang Zhao:** Supervision, Conceptualization, Writing - review & editing. **Zhao Min:** Formal analysis, Investigation. **Hejun Zhu:** Project administration, Supervision, Validation, Writing - original draft. **Xinzheng Ma** and **Zheng Li:** Data curation. **Wei Lu:** Methodology, Conceptualization. **Xingkun Chen:** Formal analysis. **Linbin Ying:** Density functional theory calculations. **Ronghe Lin:** Formal analysis, Writing - review & editing. **Yu Meng:** Density functional theory calculations. **Yuan Lyu:** Formal analysis, Investigation. **Li Yan:** Project administration, Resources. **Yunjie Ding:** Supervision, Project administration, Writing -

review & editing.

Declaration of Competing Interest

The authors declare that they have no known competing financial interests or personal relationships that could have appeared to influence the work reported in this paper.

Data availability

No data was used for the research described in the article.

Acknowledgements

We greatly appreciate the financial support by the National Natural Science Foundation of China (No. 22002151, No. 22162028 and No. 22102147), the Strategic Priority Research Program of the Chinese Academy of Sciences (Grant No. XDA 29050300), National Key Research and Development Program of China (No. 2023YFB4103100), Young Elite Scientists Sponsorship Program by CAST (No. 2023QNRC001), Zhejiang Provincial Natural Science Foundation of China (No. LQ21B030009) and Key Research and Development Program of Shaanxi (No. 2022GY-204). We acknowledge Professor Yuefeng Liu for advices and discussions on the manuscript.

Appendix A. Supporting information

Supplementary data associated with this article can be found in the online version at [doi:10.1016/j.apcatb.2024.123824](https://doi.org/10.1016/j.apcatb.2024.123824).

References

- [1] Q. Zhao, Z. Yan, C. Chen, J. Chen, Spinels: controlled preparation, oxygen reduction/evolution reaction application, and beyond, *Chem. Rev.* 117 (2017) 10121–10211.
- [2] X. Liu, M. Wang, H. Yin, J. Hu, K. Cheng, J. Kang, Q. Zhang, Y. Wang, Tandem catalysis for hydrogenation of CO and CO₂ to lower olefins with bifunctional catalysts composed of spinel oxide and SAPO-34, *ACS Catal.* 10 (2020) 8303–8314.
- [3] N. Li, Y. Zhu, F. Jiao, X. Pan, Q. Jiang, J. Cai, Y. Li, W. Tong, C. Xu, S. Qu, B. Bai, D. Miao, Z. Liu, X. Bao, Steering the reaction pathway of syngas-to-light olefins with coordination unsaturated sites of ZnGaO_x spinel, *Nat. Commun.* 13 (2022) 2742.
- [4] C. Dong, Z. Qu, Y. Qin, Q. Fu, H. Sun, X. Duan, Revealing the highly catalytic performance of spinel CoMn₂O₄ for toluene oxidation: involvement and replenishment of oxygen species using *in situ* designed-TP techniques, *ACS Catal.* 9 (2019) 6698–6710.
- [5] F.F. Tao, J.-j. Shan, L. Nguyen, Z. Wang, S. Zhang, L. Zhang, Z. Wu, W. Huang, S. Zeng, P. Hu, Understanding complete oxidation of methane on spinel oxides at a molecular level, *Nat. Commun.* 6 (1) (2015) 10.
- [6] T. Franken, R. Palkovits, Investigation of potassium doped mixed spinels Cu_xCo_{3-x}O₄ as catalysts for an efficient N₂O decomposition in real reaction conditions, *Appl. Catal. B Environ.* 176–177 (2015) 298–305.
- [7] Q. Hu, L. Yang, G. Fan, F. Li, Hydrogenation of biomass-derived compounds containing a carbonyl group over a copper-based nanocatalyst: insight into the origin and influence of surface oxygen vacancies, *J. Catal.* 340 (2016) 184–195.
- [8] J. Wu, J. Gao, S. Lian, J. Li, K. Sun, S. Zhao, Y.D. Kim, Y. Ren, M. Zhang, Q. Liu, Z. Liu, Z. Peng, Engineering the oxygen vacancies enables Ni single-atom catalyst for stable and efficient C-H activation, *Appl. Catal. B Environ.* 314 (2022) 121516.
- [9] L. Liu, A. Corma, Metal catalysts for heterogeneous catalysis: from single atoms to nanoclusters and nanoparticles, *Chem. Rev.* 118 (2018) 4981–5079.
- [10] A.I.M. Rabee, D. Zhao, S. Cisneros, C.R. Kreyenschulte, V. Kondratenko, S. Bartling, C. Kubis, E.V. Kondratenko, A. Brückner, J. Rabeeah, Role of interfacial oxygen vacancies in low-loaded Au-based catalysts for the low-temperature reverse water gas shift reaction, *Appl. Catal. B Environ.* 321 (2023) 122083.
- [11] Y. Nakaya, S. Furukawa, Catalysis of alloys: classification, principles, and design for a variety of materials and reactions, *Chem. Rev.* 123 (2023) 5859–5947.
- [12] T. Pinheiro Araujo, C. Mondelli, M. Agrachev, T. Zou, P.O. Willi, K.M. Engel, R. N. Grass, W.J. Stark, O.V. Safonova, G. Jeschke, S. Mitchell, J. Perez-Ramirez, Flame-made ternary Pd-In₂O₃-ZrO₂ catalyst with enhanced oxygen vacancy generation for CO₂ hydrogenation to methanol, *Nat. Commun.* 13 (2022) 5610.
- [13] F. Wang, S. He, H. Chen, B. Wang, L. Zheng, M. Wei, D.G. Evans, X. Duan, Active site dependent reaction mechanism over Ru/CeO₂ catalyst toward CO₂ methanation, *J. Am. Chem. Soc.* 138 (2016) 6298–6305.
- [14] A. Parastaei, V. Muravev, E.H. Osta, T.F. Kimpel, J.F.M. Simons, A.J.F. van Hoof, E. Uslamin, L. Zhang, J.C. Struijs, D.B. Burueva, E.V. Pokochueva, K.V. Kovtunov, I.V. Koptyug, I.J. Villar-Garcia, C. Escudero, T. Altantzis, P. Liu, A. Béché, S. Bals, N. Kosinov, E.J.M. Hensen, Breaking structure sensitivity in CO₂ hydrogenation by tuning metal–oxide interfaces in supported cobalt nanoparticles, *Nat. Catal.* 5 (2022) 1051–1060.
- [15] M. He, Y. Sun, B. Han, Green carbon science: efficient carbon resource processing, utilization, and recycling towards carbon neutrality, *Angew. Chem. Int. Ed.* 61 (2022) e202112835.
- [16] W. Wang, S. Wang, X. Ma, J. Gong, Recent advances in catalytic hydrogenation of carbon dioxide, *Chem. Soc. Rev.* 40 (2011) 3703–3727.
- [17] J. Zhong, X. Yang, Z. Wu, B. Liang, Y. Huang, T. Zhang, State of the art and perspectives in heterogeneous catalysis of CO₂ hydrogenation to methanol, *Chem. Soc. Rev.* 49 (2020) 1385–1413.
- [18] J. Artz, T.E. Muller, K. Thenert, J. Kleinekorte, R. Meys, A. Sternberg, A. Bardow, W. Leitner, Sustainable conversion of carbon dioxide: an integrated review of catalysis and life cycle assessment, *Chem. Rev.* 118 (2018) 434–504.
- [19] M.D. Porosoff, B. Yan, J.G. Chen, Catalytic reduction of CO₂ by H₂ for synthesis of CO, methanol and hydrocarbons: challenges and opportunities, *Energy Environ. Sci.* 9 (2016) 62–73.
- [20] H. Chen, Z. Zhao, G. Wang, Z. Zheng, J. Chen, Q. Kuang, Z. Xie, Dynamic phase transition of iron oxycarbide facilitated by Pt nanoparticles for promoting the reverse water gas shift reaction, *ACS Catal.* (2021) 14586–14595.
- [21] A.M. Bahmanpour, M. Signorile, O. Kröcher, Recent progress in syngas production via catalytic CO₂ hydrogenation reaction, *Appl. Catal. B Environ.* 295 (2021) 120319.
- [22] X. Zhang, X. Zhu, L. Lin, S. Yao, M. Zhang, X. Liu, X. Wang, Y.-W. Li, C. Shi, D. Ma, Highly dispersed copper over β -Mo₂C as an efficient and stable catalyst for the reverse water gas shift (RWGS) reaction, *ACS Catal.* 7 (2016) 912–918.
- [23] W. Gao, S. Liang, R. Wang, Q. Jiang, Y. Zhang, Q. Zheng, B. Xie, C.Y. Toe, X. Zhu, J. Wang, L. Huang, Y. Gao, Z. Wang, C. Jo, Q. Wang, L. Wang, Y. Liu, B. Louis, J. Scott, A.C. Roger, R. Amal, H. He, S.E. Park, Industrial carbon dioxide capture and utilization: state of the art and future challenges, *Chem. Soc. Rev.* 49 (2020) 8584–8686.
- [24] F. Marques Mota, D.H. Kim, From CO₂ methanation to ambitious long-chain hydrocarbons: alternative fuels paving the path to sustainability, *Chem. Soc. Rev.* 48 (2019) 205–259.
- [25] J. Cored, A. Garcia-Ortiz, S. Iborra, M.J. Climent, L. Liu, C.H. Chuang, T.S. Chan, C. Escudero, P. Concepcion, A. Corma, Hydrothermal synthesis of ruthenium nanoparticles with a metallic core and a ruthenium carbide shell for low-temperature activation of CO₂ to methane, *J. Am. Chem. Soc.* 141 (2019) 19304–19311.
- [26] W. Li, X. Nie, X. Jiang, A. Zhang, F. Ding, M. Liu, Z. Liu, X. Guo, C. Song, ZrO₂ support imparts superior activity and stability of Co catalysts for CO₂ methanation, *Appl. Catal. B Environ.* 220 (2018) 397–408.
- [27] K. Feng, J. Tian, M. Guo, Y. Wang, S. Wang, Z. Wu, J. Zhang, L. He, B. Yan, Experimentally unveiling the origin of tunable selectivity for CO₂ hydrogenation over Ni-based catalysts, *Appl. Catal. B Environ.* 292 (2021) 120191.
- [28] A.M. Bahmanpour, F. Héroguel, M. Kılıç, C.J. Baranowski, L. Artiglia, U. Röthlisberger, J.S. Luterbacher, O. Kröcher, Cu-Al spinel as a highly active and stable catalyst for the reverse water gas shift reaction, *ACS Catal.* 9 (2019) 6243–6251.
- [29] L. Song, H. Wang, S. Wang, Z. Qu, Dual-site activation of H₂ over Cu/ZnAl₂O₄ boosting CO₂ hydrogenation to methanol, *Appl. Catal. B Environ.* 322 (2023) 122137.
- [30] J. Wang, G. Zhang, J. Zhu, X. Zhang, F. Ding, A. Zhang, X. Guo, C. Song, CO₂ hydrogenation to methanol over In₂O₃-based catalysts: from mechanism to catalyst development, *ACS Catal.* 11 (2021) 1406–1423.
- [31] C. Yang, S. Liu, Y. Wang, J. Song, G. Wang, S. Wang, Z.J. Zhao, R. Mu, J. Gong, The interplay between structure and product selectivity of CO₂ hydrogenation, *Angew. Chem. Int. Ed.* 58 (2019) 11242–11247.
- [32] A.M. Bahmanpour, F. Héroguel, M. Kılıç, C.J. Baranowski, P. Schouwink, U. Röthlisberger, J.S. Luterbacher, O. Kröcher, Essential role of oxygen vacancies of Cu-Al and Co-Al spinel oxides in their catalytic activity for the reverse water gas shift reaction, *Appl. Catal. B Environ.* 266 (2020) 118669.
- [33] N.H.M.D. Dostagir, R. Rattanawan, M. Gao, J. Ota, J.-y Hasegawa, K. Asakura, A. Fukouka, A. Shrotri, Co single atoms in ZrO₂ with inherent oxygen vacancies for selective hydrogenation of CO₂ to CO, *ACS Catal.* (2021) 9450–9461.
- [34] J. Wang, C. Tang, G. Li, Z. Han, Z. Li, H. Liu, F. Cheng, C. Li, High-performance M_xZrO_x (M_x = Cd, Ga) solid-solution catalysts for CO₂ hydrogenation to methanol, *ACS Catal.* 9 (2019) 10253–10259.
- [35] Y. Wang, Z. Chen, P. Han, Y. Du, Z. Gu, X. Xu, G. Zheng, Single-atomic Cu with multiple oxygen vacancies on ceria for electrocatalytic CO₂ reduction to CH₄, *ACS Catal.* 8 (2018) 7113–7119.
- [36] C. Dong, R. Mu, R. Li, J. Wang, T. Song, Z. Qu, Q. Fu, X. Bao, Disentangling local interfacial confinement and remote spillover effects in oxide–oxide interactions, *J. Am. Chem. Soc.* 145 (2023) 17056–17065.
- [37] H. Liu, W. Jia, X. Yu, X. Tang, X. Zeng, Y. Sun, T. Lei, H. Fang, T. Li, L. Lin, Vitamin C-assisted synthesized Mn–Co oxides with improved oxygen vacancy concentration: boosting lattice oxygen activity for the air-oxidation of 5-(hydroxymethyl)furfural, *ACS Catal.* 11 (2021) 7828–7844.
- [38] Y.J. Wong, M.K. Koh, N.F. Khairudin, S. Ichikawa, Y. Morikawa, A.R. Mohamed, Development of Co supported on Co-Al spinel catalysts from exsolution of amorphous Co-Al oxides for carbon dioxide reforming of methane, *ChemCatChem* 11 (2019) 5593–5605.
- [39] M. Zhao, Y. Li, Z. Zhao, Y. Lyu, W. Lu, H. Zhu, Y. Ding, Mn doping of Co-Al spinel as Fischer-Tropsch catalyst support, *Appl. Catal. A Gen.* 624 (2021) 118308.

[40] X. Liu, L. Zhao, H. Xu, Q. Huang, Y. Wang, C. Hou, Y. Hou, J. Wang, F. Dang, J. Zhang, Tunable cationic vacancies of cobalt oxides for efficient electrocatalysis in Li–O₂ batteries, *Adv. Energy Mater.* 10 (2020) 2001415.

[41] G. Ou, Y. Xu, B. Wen, R. Lin, B. Ge, Y. Tang, Y. Liang, C. Yang, K. Huang, D. Zu, R. Yu, W. Chen, J. Li, H. Wu, L.M. Liu, Y. Li, Tuning defects in oxides at room temperature by lithium reduction, *Nat. Commun.* 9 (2018) 1302.

[42] C.M. Álvarez-Docio, J.J. Reinoso, A. Del Campo, J.F. Fernández, Investigation of thermal stability of 2D and 3D CoAl₂O₄ particles in core-shell nanostructures by Raman spectroscopy, *J. Alloy. Compd.* 779 (2019) 244–254.

[43] Y. Ding, C.C. Hu, W.Q. Sheng, K.X. Song, B. Liu, Crystal structure, microwave dielectric properties, and dielectric resonant antenna studies of novel low-permittivity CoAl₂O₄ spinel ceramics, *J. Mater. Sci.* 32 (2021) 22813–22821.

[44] B. Zhang, S. Zhang, B. Liu, Effect of oxygen vacancies on ceria catalyst for selective catalytic reduction of NO with NH₃, *Appl. Surf. Sci.* 529 (2020).

[45] X. Chen, X. Chen, E. Yu, S. Cai, H. Jia, J. Chen, P. Liang, In situ pyrolysis of Ce-MOF to prepare CeO₂ catalyst with obviously improved catalytic performance for toluene combustion, *Chem. Eng. J.* 344 (2018) 469–479.

[46] Y. Li, W. Lu, Z. Zhao, M. Zhao, Y. Lyu, L. Gong, H. Zhu, Y. Ding, Tuning surface oxygen group concentration of carbon supports to promote Fischer-Tropsch synthesis, *Appl. Catal. A Gen.* 613 (2021) 118017.

[47] J. Li, C. Li, S. Feng, Z. Zhao, H. Zhu, Y. Ding, Atomically dispersed Zn-N_x sites in N-doped carbon for reductive N-formylation of nitroarenes with formic acid, *ChemCatChem* 12 (2020) 1546–1550.

[48] Y. Li, Z. Zhao, W. Lu, H. Zhu, F. Sun, B. Mei, Z. Jiang, Y. Lyu, X. Chen, L. Guo, T. Wu, X. Ma, Y. Meng, Y. Ding, Single-atom Co-N-C catalysts for high-efficiency reverse water-gas shift reaction, *Appl. Catal. B Environ.* 324 (2023) 122298.

[49] W. Li, G. Zhang, X. Jiang, Y. Liu, J. Zhu, F. Ding, Z. Liu, X. Guo, C. Song, CO₂ hydrogenation on unpromoted and M-promoted Co/TiO₂ catalysts (M = Zr, K, Cs): effects of crystal phase of supports and metal-support interaction on tuning product distribution, *ACS Catal.* 9 (2019) 2739–2751.

[50] J.L. Dechen Song, Qin Cai, In situ diffuse reflectance FTIR study of CO adsorbed on a cobalt catalyst supported by silica with different pore sizes, *J. Phys. Chem. C* 111 (2007) 18970–18979.

[51] C. Vogt, E. Groeneveld, G. Kamsma, M. Nachtegaal, L. Lu, C.J. Kiely, P.H. Berben, F. Meirer, B.M. Weckhuysen, Unravelling structure sensitivity in CO₂ hydrogenation over nickel, *Nat. Catal.* 1 (2018) 127–134.